ADVANCED FUNCTIONAL MATERIALS
www.afm-journal.de

Shape Control of Mn_3O_4 Nanoparticles on Nitrogen-Doped Graphene for Enhanced Oxygen Reduction Activity

*Jingjing Duan, Sheng Chen, Sheng Dai, and Shi Zhang Qiao**

Three kinds of Mn_3O_4 nanoparticles with different shapes (spheres, cubes, and ellipsoids) are selectively grown on nitrogen-doped graphene sheets through a two-step liquid-phase procedure. These non-precious hybrid materials display an excellent ORR activity and good durability. The mesoporous microstructure, nitrogen doping, and strong bonding between metal species and doped graphene are found to facilitate the ORR catalytic process. Among these three kinds of Mn_3O_4 particles, the ellipsoidal particles on nitrogen-doped graphene exhibit the highest ORR activity with a more positive onset-potential of –0.13 V (close to that of Pt/C, –0.09 V) and a higher kinetic limiting current density (J_K) of 11.69 mA cm^{-2} at –0.60 V. It is found that the ORR performance of hybrid materials can be correlated to the shape of Mn_3O_4 nanocrystals, and specifically to the exposed crystalline facets associated with a given shape. The shape dependence of Mn_3O_4 nanoparticles integrated with nitrogen-doped graphene on the ORR performance, reported here for the first time, may advance the development of fuel cells and metal-air batteries.

1. Introduction

Heterogeneous catalytic reactions usually involve adsorption of reactants and desorption of products on the surface of solid catalysts.[1,2] Therefore, a catalyst particle with an anisotropic shape can greatly modify the catalytic performance by selectively exposing specific crystal facets, which is termed as shape-dependent heterogeneous catalysis. In the case of shape-dependent catalysis, the ultimate goal is to design and synthesize catalysts by decreasing the less-reactive crystal facets and increasing the more-reactive ones, which leads to better catalytic performance. Recently, the sluggish heterogeneous catalysis-oxygen reduction reaction (ORR) has been reported to be the main challenge in the commercial success of fuel cells and metal-air batteries.[3,4] Pt-based materials are known as the most active ORR electrocatalysts, but their large-scale application has been constrained by the scarcity, prohibitive cost and limited durability of noble metals.[5,6] Therefore, low-cost ORR catalysts with competitive activity and durability are highly desirable, such as non-precious metal and metal-free catalysts.[4,7]

J. J. Duan, Dr. S. Chen, Prof. S. Dai, Prof. S. Z. Qiao
School of Chemical Engineering
The University of Adelaide
SA, 5005, Australia
E-mail: s.qiao@adelaide.edu.au

DOI: 10.1002/adfm.201302940

Non-precious metal oxides have been actively pursued as electrocatalysts because of their low price, abundance and environmental compatibility.[8–11] As compared to other metal oxides, Mn_3O_4 is active for several redox reactions due to its polymorphism and coexistence of mix-valence.[12,13] However, the electroconductivity of Mn_3O_4 is poor and nanoparticles usually suffer from dissolution and agglomeration during catalytic processes, which can compromise kinetics and reduce ORR activity. Therefore, supports like doped graphene are usually employed to improve the electroconductivity, catalytic stability and even activity.[14] As compared to other supports, graphene, as a two-dimensional sp^2-hybridized carbon sheet, has attracted a considerable attention because of its excellent electrical conductivity, high surface area and good chemical stability. Moreover, doped graphene with heteroatoms like nitrogen has displayed an excellent ORR performance, which is related to the introduced asymmetry spin density and charge density through heteroatom doping.[15,16] This effect would not fade even after long-time operation because the doped heteroatoms are covalently bonded to carbon, which guarantees a good durability of such hybrid material. The latter, consisting of Mn_3O_4 and nitrogen-doped graphene, is inexpensive, eco-friendly, highly active and stable ORR catalyst as compared to other composites.[9,17]

Shape-dependence in catalysis has been usually explained in terms of different active sites present on different exposed crystal facets of catalysts.[1,2,18] During ORR catalytic process, the surface atomic structures present on the exposed crystal facets are critically important for oxygen adsorption. To date, the dependence of ORR on the shape of electrocatalytic materials has been mainly explored for precious metals and their alloys.[19,20] The investigation of the shape-dependence of the ORR catalysis promoted by non-precious transition metal oxides is promising and highly demanded due to their crystallographic polymorphism, which is rarely reported, but can be utilized for improving catalytic performance.[21]

In this work, we synthesized three kinds of Mn_3O_4 nanoparticles differing in the shape (spheres, cubes, and ellipsoids) and exposed crystal facets, integrated them with nitrogen-doped graphene, and investigated the shape-dependence of the ORR process. The adopted liquid phase method to dope nitrogen into graphene sheets is eco-friendly, energy-saving and non-hazardous as compared to the widely used vapor phase process.

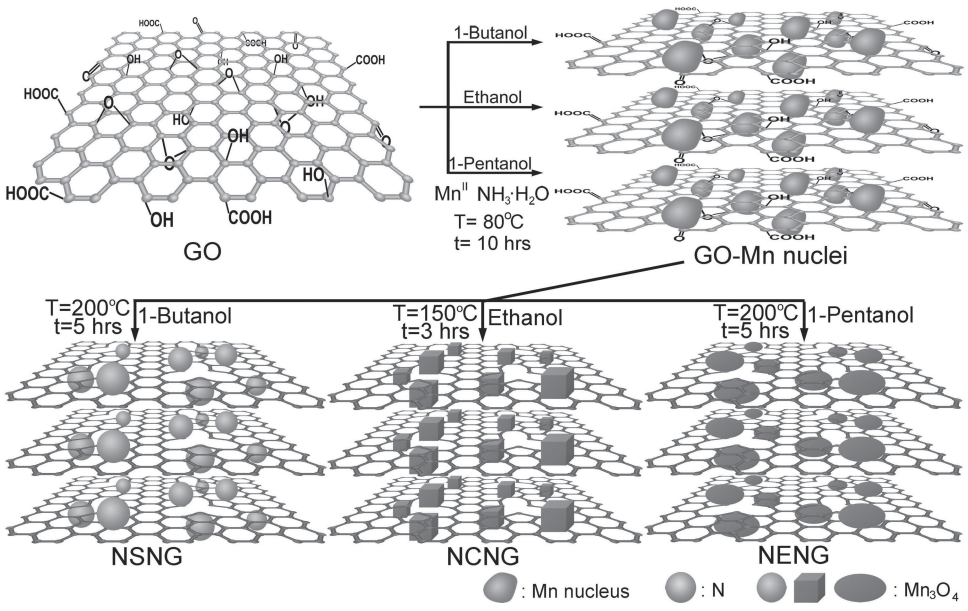

Figure 1. Schematic illustration of the preparation procedure of Mn_3O_4 nanoparticles with three different morphologies on nitrogen-doped graphene sheets.

The mesoporous architecture resulting from nanoparticle assembly is favourable to oxygen adsorption and molecular transport during the ORR process. The strong bonding between metal species and doped graphene could prevent nanoparticles from agglomeration and improve the electroconductivity.[22] The study of the ORR activity of transition metal oxide nanocrystals in relation to their shape opens new possibilities in optimizing the ORR performance in fuel cells and metal-air batteries.

2. Results and Discussion

2.1. Materials Synthesis and Characterization

The synthesis process is illustrated in **Figure 1**. Graphene oxide sheets (denoted as GO, Figure S1 in Supporting Information) merged with $Mn(AC)_2$ and ammonia in different solvents were first treated in water bath at 80 °C for 10 h. During this process, irregular Mn_3O_4 nuclei were formed on GO sheets via heterogeneous nucleation. The as-obtained GO-Mn nuclei solution was further solvothermally treated in an autoclave. In this process, GO was deoxygenated and nitrogen was doped into graphene sheets at a high pressure and elevated temperature;[23] Simultaneously, Mn_3O_4 nuclei continued to grow into sphere, cube, and ellipsoid-like nanoparticles under different reaction conditions.

The structure and morphology of the hybrid materials were examined. Firstly, Mn_3O_4 quasi-nanospheres on nitrogen-doped graphene (denoted as NSNG) were obtained using 1-butanol as a solvent at 200 °C for 5 h (**Figure 2**a and Supporting Information, Figure S2a,b). Transmission electron microscope (TEM) images show that the size of these nanospheres ranges from several to 20 nm. The high resolution TEM (HRTEM) image shows that each nanosphere is a single-crystal dominant Mn_3O_4 nanoparticle with an inter-planar spacing of 0.272 nm corresponding to the (103) plane of hausmannite Mn_3O_4 (Figure 2b).[24] The electron diffraction (ED) pattern of nanospheres (inset of Figure 2b) is consistent with hausmannite Mn_3O_4. Interestingly, when the solvothermal synthesis was carried out in ethanol at 150 °C and 3 h, Mn_3O_4 quasi-nanocubes with sizes from 5 to 20 nm were obtained on nitrogen-doped graphene (denoted as NCNG, Figure 2c and Supporting Information, Figure S2c,d). The HRTEM image of NCNG (Figure 2d) displays inter-planar spacings of 0.284 nm and 0.234 nm, which can be assigned to (200) and (004) planes of hausmannite Mn_3O_4, which is consistent with the ED pattern (inset of Figure 2d). Furthermore, Mn_3O_4 quasi-nanoellipsoids on nitrogen-doped graphene (denoted as NENG) were prepared in 1-pentanol at 200 °C for 5 h (Figure 2e and Supporting Information, Figure S2e,f). The nanoellipsoids are about 5 nm in width and 20 nm in length. The HRTEM image of NENG shows inter-planar distances of 0.307 nm and 0.272 nm, corresponding to (112) and (103) planes of hausmannite (Figure 2f). The ED pattern of nanoellipsoids can also be ascribed to hausmannite Mn_3O_4, as shown in the inset of Figure 2f. The sizes of three types of Mn_3O_4 nanoparticles can be considered as similar. The disparities in the nanoparticle sizes observed from TEM and SEM images result from agglomeration of primary particles (TEM testing), which is also called as secondary particles (SEM testing).

The X-ray diffraction (XRD) patterns of the samples (**Figure 3**a) can all be assigned to tetragonal Mn_3O_4 structure (hausmannite, $I4_1/amd$, $a_0 = b_0 = 5.76$ Å, and $c_0 = 9.47$ Å; JCPDS card no. 24-0734), which is in accordance with the ED patterns.[24–26] The Raman spectra display signals of Mn–O band (650 cm^{-1}) from Mn_3O_4, D band (1360 cm^{-1}), G band (1600 cm^{-1}), and combination of D+G band (2900 cm^{-1}) from graphene, confirming the presence of graphene in these hybrid materials (Figure 3b).[27,28] The high ratios of I_D/I_G (1.06, 1.1,

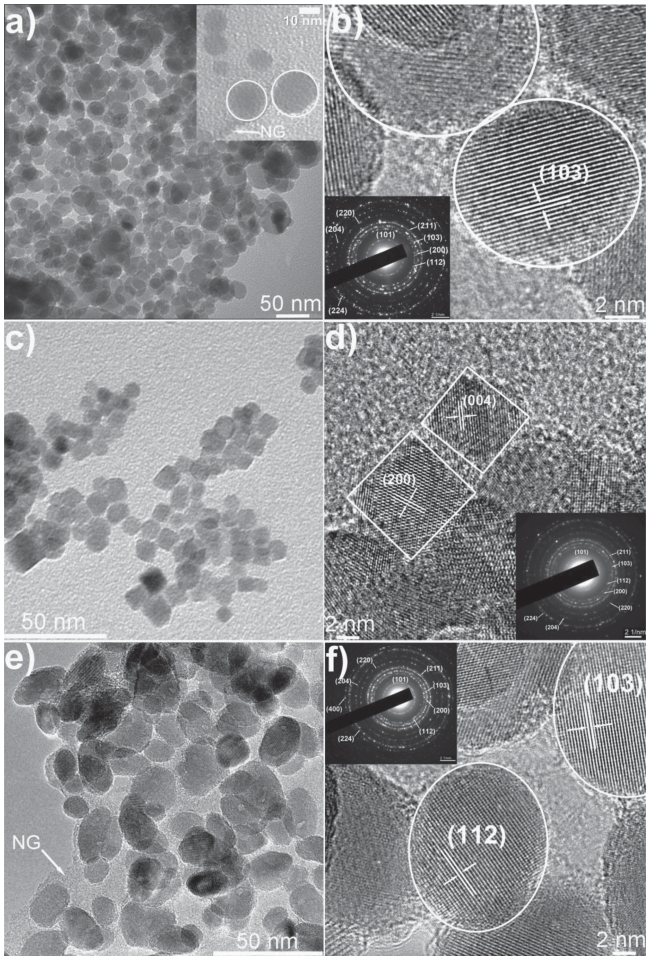

Figure 2. a) TEM images, b) HRTEM image of NSNG (inset is ED pattern); c) TEM image, d) HRTEM image of NCNG (inset is the ED pattern); e) TEM image, f) HRTEM image of NENG (inset is the ED pattern).

and 1.2 for NSNG, NCNG and NENG) clearly indicate the presence of structural defects in graphene sheets due to nitrogen doping. Furthermore, the mass ratios of Mn_3O_4 in NSNG, NCNG, and NENG are similar as determined by thermogravimetric analysis (TGA), which are 83 wt%, 80 wt%, and 84 wt%. (Figure S3, Supporting Information).

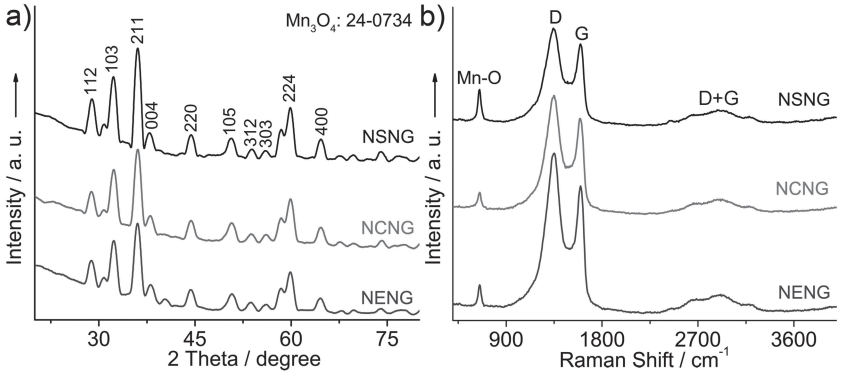

Figure 3. a) XRD patterns and b) Raman spectra of NSNG, NCNG, and NENG.

Nitrogen adsorption isotherms were measured to investigate the pore structure of as-prepared hybrid materials. The isotherms of all samples are type-IV with a distinct hysteresis loop at relative pressures (P/P_0) from 0.45 to 1.0 (**Figure 4**a), suggesting the presence of mesopores in these materials. The pore size distribution (PSD) curves of NENG and NSNG are centred at ≈42 nm which is larger than that of NCNG (≈22 nm), further confirming their mesoporous structure (Figure 4b).[29] The Brunauer-Emmett-Teller (BET) surface area and the total pore volume of NENG was estimated to be 85 m^2 g^{-1} and 0.19 cm^3 g^{-1}, in contrast to those of NSNG (47 m^2 g^{-1} and 0.15 cm^3 g^{-1}) and NCNG (164 m^2 g^{-1} and 0.35 cm^3 g^{-1}). The mesoporous architecture of the hybrid materials resulting from nanoparticle assembly can facilitate oxygen adsorption and molecular transport during the ORR process.

X-ray photoelectron spectroscopy (XPS) survey scan of NENG (**Figure 5**a, 0–1000 eV) indicates the presence of manganese, carbon, oxygen and nitrogen. The deconvolution of corresponding N 1s spectrum (Figure 5b) indicates the existence of three nitrogen structures, that is, pyridinic at 398.7 eV, pyrrolic at 400.4 eV and graphitic at 401.5 eV.[23,30] The deconvolution of C 1s spectrum (Figure 5c) shows the presence of nonoxygenated carbon at 284.2 eV, C–O at 287.0 eV, and C=O at 288.8 eV. In the Mn 2p spectrum, a $2p_{3/2}$-$2p_{1/2}$ doublet at 640.3 and 651.9 eV with a splitting width of 11.6 eV is in agreement with previous report (Figure 5d).[31] The estimated N/C ratio in NENG is 6.65%. XPS spectra of NSNG and NCNG are shown in Supporting Information, Figures S4,S5, with calculated N/C ratios of 4.75% and 7.21%. Furthermore, the as-prepared samples were characterized by Fourier transform infrared spectroscopy (FTIR, Figure S6, Supporting Information). The FTIR spectrum of GO displays characteristic bands of stretching vibration of O–H (3400 cm^{-1}), C=O (1725 cm^{-1}), and C–O (1070 cm^{-1}). However, these peaks disappear in the FTIR spectra of three hybrid samples, indicating the removal of these oxygen-containing groups. Importantly, new peaks were identified at 1570 cm^{-1} for all three samples, probably due to the newly formed C–N bond after nitrogen doping.[32,33] The observed contradiction between XPS and FTIR data resulted from the different sensitivity of these two analysis tools.

The formation mechanism of Mn_3O_4 nanoparticles with different shapes on nitrogen-doped graphene was further investigated. Apart from the oxygen-containing functional groups on GO, the nitrogen-doped graphene sheets can also act as anchoring sites for metal oxide nanoparticles, which result in a strong coupling between metal species and N-doped graphene that can effectively prevent metal oxide nanoparticles from agglomeration and re-crystallization into big particles.[22,34] For the purpose of comparison the corresponding samples without nitrogen doping were also prepared (Supporting Information, Figure S7, denoted as NSG, NCG, and NEG); in these three samples, Mn_3O_4 nanocrystals re-grow into large particles due to Ostwald ripening, which resulted in a poor monodispersity. Generally, the surface energy plays a vital role in the anisotropic growth of nanoparticles after

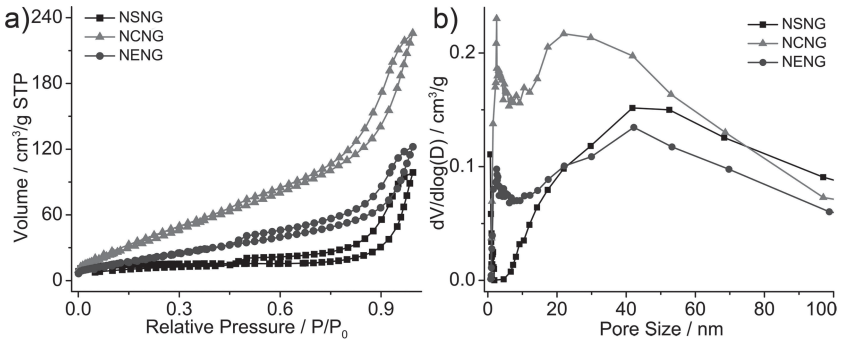

Figure 4. a) Nitrogen adsorption-desorption isotherms, and b) pore size distribution curves of NSNG, NCNG, and NENG.

nucleation, and the growth rate is exponentially proportional to the surface energy.[25,35–37] At a high temperature (200 °C) and relatively long growth duration (5 h) in 1-butanol, the growth of nanocrystals is complete and the thermodynamically favourable sphere-like Mn_3O_4 nanoparticles are obtained, which is stabilized by some high Miller index facets, driven by autonomous minimization of the surface energy. According to the Wuff facet theory, the crystal growth should occur rapidly on high-free-energy facets, resulting in crystals with low-free-energy facets.[25] Therefore, at a lower temperature (150 °C) and a shorter reaction time (3 h) in ethanol, the cube-like morphology is observed, which was stabilized with low Miller-index facets ((100), (010), and (001)). Moreover, replacing 1-butanol by 1-pentanol the high temperature (200 °C) with sufficient growth duration (5 h), the crystal growth rate on high-free-energy facets increased because of the improved reactivity of ions in solution due to the decreased solvent polarity, resulting in more low-Miller-index facets, so ellipsoid-like nanoparticles were formed (sample NENG).[38] As a result, the ellipsoidal sample has the highest percentage of (001) facet, which features the lowest surface energy in three samples.[39]

2.2. Electrocatalytic Analysis

ORR catalytic activities of three samples were examined by cyclic voltammetry (CV) on a rotating disk electrode (RDE) both in N_2 and O_2-saturated 0.1 M KOH solution. CV curves of all the samples recorded in N_2-saturated electrolyte show no obvious peaks, indicating that ORR did not occur (Figure S8, Supporting Information). In contrast, the CV curve of NENG in O_2-saturated electrolyte shows one ORR reduction peak at –0.30 V with a current density of 1.83 mA cm^{-2}; the ORR reduction peak for NSNG is at –0.37 V with a current density of 1.30 mA cm^{-2}, while this peak for NCNG is at –0.38 V with a current density of 1.36 mA cm^{-2} (**Figure 6**a). The observed ORR peak for each sample originates from one-step four-electron oxygen reduction pathway.[40,41] Although the peak potential of NENG (-0.30 V) is more negative than that of Pt/C (–0.19 V), its reaction current density is higher than that of Pt/C (1.64 mA cm^{-2}, Figure S9a, Supporting Information). To obtain further insight into ORR activities of these three samples, the linear sweep voltammograms (LSVs) recorded in O_2-saturated electrolyte on RDE at 1600 rpm were compared (Figure 6b). NSNG exhibits an onset-potential of –0.18 V and a current density of 2.47 mA cm^{-2} at –0.6 V; NCNG shows an onset-potential of –0.16 V and a current density of 3.41 mA cm^{-2} at –0.6 V; and the LSV of NENG displays an onset-potential of –0.13 V close to that of Pt/C (–0.09 V, Figure S9b, Supporting Information) and a high current density of 3.70 mA cm^{-2} at –0.6 V. As evidenced by CV and LSVs, NENG displays the highest ORR activity among these three samples, which is reflected by the most positive onset-potential and highest current density. The onset-potential of NENG is more positive than those reported for Fe_3O_4/nitrogen-doped graphene, CoO/carbon nanotube, and $Co(OH)_2$/graphene hybrid materials; and its current density is also higher than those reported for Fe_3O_4/nitrogen-doped graphene and $Co(OH)_2$/graphene hybrid materials.[9,42,43]

To quantitatively understand ORR activities of these three samples, the Koutecky-Levich plots (K-L, J^{-1} vs $\omega^{-1/2}$, Figure 6c

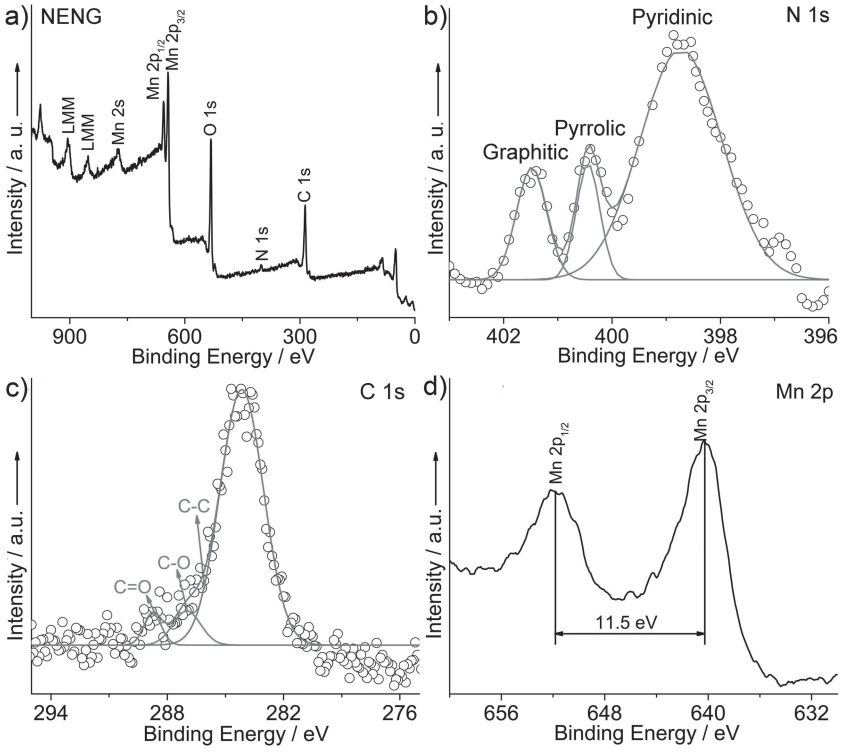

Figure 5. XPS spectra of NENG. a) Survey scan, b) high resolution N 1s spectrum, c) C 1s spectrum, and d) Mn 2p spectrum.

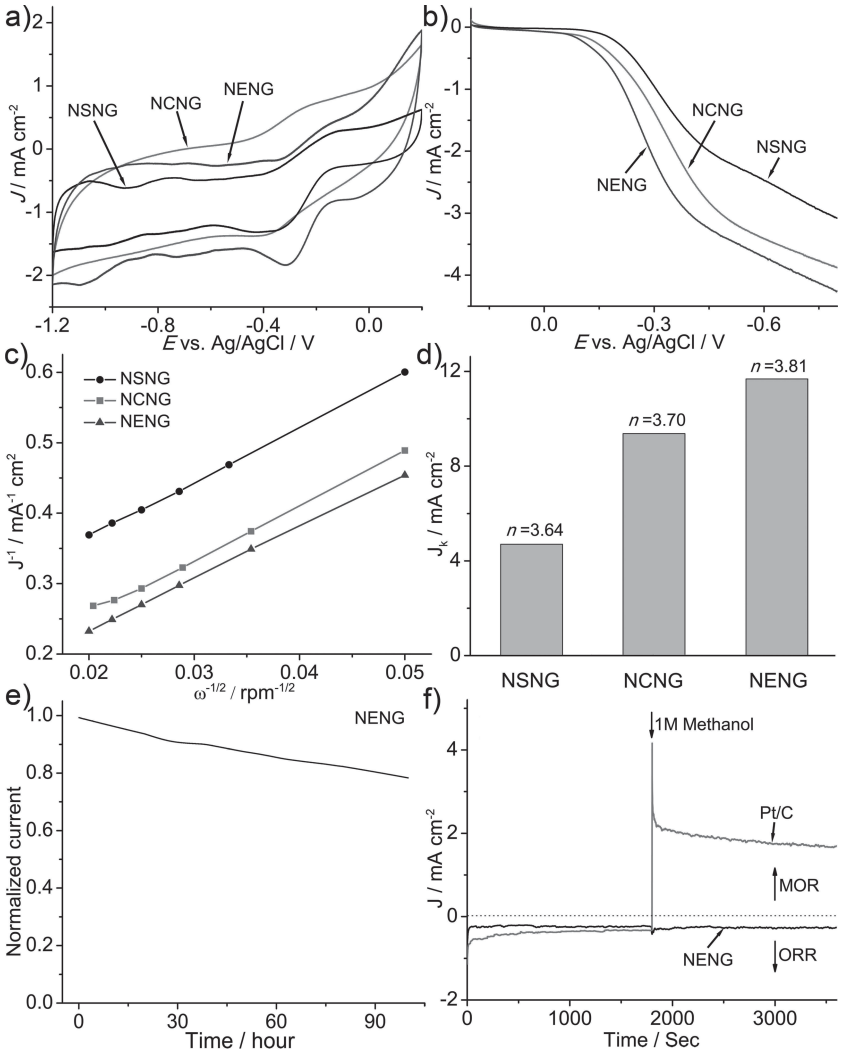

Figure 6. a) CV curves, b) LSVs at a sweep rate of 5 mV s^{-1}, c) the calculated K-L plots and d) kinetic limiting current density (J_K) and electron transfer number (n) of NCNG, NSNG, and NENG; e) Chronoamperometric response (i–t) of NENG, f) i–t of NENG and Pt/C before and after the addition of 1 M Methanol. The tests were conducted in O_2-saturated 0.1 M KOH solution at –0.35 V. Catalyst loading was 0.1 mg cm^{-2} for all samples.

To further understand the ORR activity, the detailed LSVs of three samples at different rotating speeds from 0 to 2500 rpm between 0.2 and –0.8 V were recorded (Figure S10a,c,e, Supporting Information). LSVs measured on NENG exhibit a typical increasing current with higher rotation speeds at the same potentials because of the shortened diffusion distance at higher speeds (Figure S10e, Supporting Information).[44,45] Detailed LSVs of NSNG and NCNG show similar behaviour. The K-L plots of NENG estimated from its LSVs from –0.4 V to –0.8 V display good linearity; but the linearity of K-L plots for NSNG and NCNG is not as good as that of NENG (Figure S10b,d,f, Supporting Information).

In addition, the long-time stability of NENG was estimated using chronoamperometric response in O_2-saturated 0.1 M KOH solution at –0.3 V (Figure 6e). NENG exhibited an excellent stability, retaining 79% of the initial current even after 100 hrrunning. This performance is much better than that of commercial Pt/C catalyst, which lost almost 50% current after 60 h running.[29] The tolerance of NENG to methanol crossover was also measured to test the selectivity towards ORR with the addition of 1 M methanol (Figure 6f). The current density of NENG displayed no obvious decrease after the addition of methanol, suggesting a high selectivity to ORR. In contrast, commercial Pt/C always exhibits a distinct methanol oxidation reaction (MOR) after the introduction of methanol, indicating that Pt/C is very sensitive to methanol crossover.[29] The excellent long-term stability as well as high selectivity to ORR further suggest that NENG is a very promising ORR electrocatalyst for direct methanol fuel cells.

and Supporting Information, Figures S9c,S10) were calculated from LSVs and compared at –0.6 V at various rotating speeds. All K-L plots display good linearity.[44,45] In particular, NENG shows the highest ORR current density, followed by those obtained for NCNG and NSNG (Figure 6c). Furthermore, electron transfer numbers (n) and kinetic limiting current density (J_K) were estimated from the slopes and the intercepts of linear K-L plots (Figure 6d). NENG shows the largest n value of 3.81 (close to that of Pt/C, 3.96, Figure S9d, Supporting Information) and the highest J_K value of 11.69 mA cm^{-2} at –0.6 V, as compared to those of NCNG (3.70 and 9.38 mA cm^{-2}) and NSNG (3.64 and 4.70 mA cm^{-2}). The n values for all three samples are close to 4, suggesting that the efficient four electron reduction dominates the catalytic processes on these hybrid materials. Obviously, the largest electron transfer number and the highest kinetic limiting current density further confirm the best ORR performance of NENG.

The density effect of Mn_3O_4 nanoparticles on the ORR activity was also investigated. NENG-1 and NENG-2 were prepared using the same method with NENG but with 1 mL and 0.5 mL of 0.2 M $Mn(AC)_2$, so as NCNG-1, NCNG-2, and NSNG-1, NSNG-2. As shown in Supporting Information Table S1 and Figures S11,S12,S13, lowering the Mn loading in Mn_3O_4/N-graphene catalysts with different shapes led to reduction in the ORR activity, suggesting that the active reaction sites in our hybrid materials could be related to metal oxide nanoparticles. The optimal nanoparticle loading in the case of ellipsoidal samples (NENG) is 56.7 wt% of Mn (78.7 wt% of Mn_3O_4) determined by EDS (energy-dispersive X-ray spectroscopy), which is a little lower than 84 wt% of Mn_3O_4 obtained by TGA because of the introduced Pt coating and carbon support for SEM testing. For cubic samples, the optimal nanoparticle population is obtained in NCNG with 61.0 wt% of Mn (84.7 wt% of Mn_3O_4), which is close to the TGA result (80 wt% of Mn_3O_4). The optimal nanoparticle loading in the case of spherical

samples (NSNG) is 54.5 wt% of Mn (75.7 wt% of Mn_3O_4) which is also close to the result measured by TGA (83 wt% of Mn_3O_4). Note that the N/C at% of NENG, NCNG and NSNG obtained by EDS are 1.23, 1.43, and 1.02, which are similar.

The excellent ORR performance of these non-precious hybrid materials can be attributed to the mesoporous architecture, nitrogen doping, introduced asymmetry charge and spin density, and strong coupling between metal species and doped graphene.[17] Specifically, the mesoporous structure can boost the mass transport during catalytic process; the unbalanced charge distribution resulting from nitrogen doping is greatly favourable to O_2 adsorption; a strong bonding between doped graphene and metal species can facilitate the electron transfer, and it is also a guarantee for the good durability. The different ORR activities of NENG, NCNG and NSNG can be attributed to various shapes of Mn_3O_4 nanoparticles in the hybrid materials. Note that (001) facets with Mn_2O_4 termination (Mn^{IV}) in Mn_3O_4 nanocrystals were shown to be favourable to catalytic processes due to high oxidation valence and strong ability to form a redox couple.[46,47] The prominent ORR activity of NENG with (001) facet dominant Mn_3O_4 nanoparticles is probably related to the facile adsorption of oxygen on (001) facets of Mn_3O_4 nanocrystals during ORR process. As a result, the ellipsoid-like Mn_3O_4 with highly exposed (001) facets displayed the highest ORR performance as compared to the cube-like sample with facets of (100), (010), and (001), and the most thermodynamically stable sphere-like sample with some high Miller index facets.

3. Conclusions

In summary, Mn_3O_4 nanoparticles with three different shapes (spheres, cubes and ellipsoids) were integrated with nitrogen-doped graphene, and the shape effect of these transition metal oxide particles on the ORR activity was studied in alkaline electrolytes. These non-precious hybrid materials exhibited excellent ORR performance, which can be ascribed to the mesoporous architecture, nitrogen doping and strong covalent bonding between doped graphene and metal species. Especially, the hybrid material with ellipsoid-like Mn_3O_4 nanocrystals on nitrogen-doped graphene displayed the best ORR activity among three samples studied, which is possibly related to the high activity of (001) facets in Mn_3O_4 nanocrystals. Significantly, an insight into the correlation between the shape of metal oxide nanocrystals and oxygen reduction catalytic activity is proposed in relation to the exposed crystal facets in metal oxide nanocrystals, which may open a new avenue for the development of low cost and environmentally friendly electrocatalysts for highly effective ORR process. This work may also advance further tuning of surface chemistry of transition metal oxides and thus, rationally design catalysts with optimal catalytic performance.

4. Experimental Section

Synthesis of Different Shaped Mn_3O_4 Nanoparticles on Nitrogen-Doped Graphene: graphite oxide was prepared by a modified Hummers' method (see supporting information).[48] A 5 mg mL^{-1} of graphite oxide aqueous solution was subjected to ultrasonic treatment (950 W, 1 h) and then centrifuged at 3000 rpm for 0.5 h. 2 mL 5 mg mL^{-1} of GO aqueous solution were added into 20 mL of solvent (1-butanol, ethanol or 1-pentanol for NSNG, NCNG and NENG synthesis, respectively), followed by the addition of 2 mL, 0.2 M $Mn(AC)_2$, and 2 mL of NH_4OH (28 wt%). The mixture was kept at 80 °C for 10 h and then loaded into a Teflon-lined stainless steel autoclave and heated at elevated temperature for several hours (200 °C for 5 h, 150 °C for 3 h and 200 °C for 5 h for NSNG, NCNG, and NENG, respectively). The samples were then washed with water and ethanol, and freeze-dried. For the samples without nitrogen doping (NSG, NCG, and NEG), the preparation method is similar as described above in the absence of NH_4OH (28 wt%). To investigate the population effect of nanoparticles on the ORR performance, 1 mL and 0.5 mL of 0.2 M $Mn(AC)_2$ were used by keeping other conditions the same to prepare the NENG, NCNG, and NSNG samples with different loadings of nanoparticles; these samples are denoted as NENG-1, NENG-2, NCNG-1, NCNG-2 and NSNG-1, NSNG-2.

Materials Characterization: TEM images were obtained on a Philips CM100 microscope at an acceleration voltage of 80 kV. High resolution TEM images were collected with JEOL JEM 2100 microscopy. SEM images were recorded on the FEI Quanta 450. For SEM testing, the powder samples were placed on carbon tabs and Pt was coated on surface of the smaple. AFM measurements were performed on NT-MDT Ntegra Solaris system. XRD patterns were collected on a powder X-ray diffractometer at 40 kV and 15 mA using Co-Kα radiation (Miniflex, Rigaku). The Raman spectra were conducted on iHR550 from HORIBA Scientific with 532 nm solid laser as an excitation source. XPS spectra were obtained using an Axis Ultra (Kratos Analytical, UK) XPS spectrometer equipped with an Al Kα source (1486.6 eV). For XPS testing, the powder samples were dispersed on carbon conductive adhesive tape to form the flat surface. Nitrogen adsorption isotherms were collected on a Tristar II 3020, Micromeritics adsorption analyzer at –196 °C. Prior to adsorption measurements, the samples were degassed at 200 °C for at least 10 h. Pore size distributions (PSD) were calculated using the adsorption branch of the isotherms by Barrett-Joyner-Halenda (BJH) method; the resulting PSD curves defined as $dV/d(\log D)$, where V is the volume adsorbed and D is the pore width, are presented in figures. The total pore volume was estimated from the adsorption volume at a relative pressure (P/P_0) of 0.99. The FTIR spectra were collected on the transmission module of a Thermo Nicolet 6700 FTIR spectrometer at 2 cm^{-1} resolution and 64 scans. TGA was measured using a Setaram Labsys Thermogravimetric Analyzer in O_2 atmosphere, over a temperature range from 20 to 520 °C with a heating rate of 10 °C min^{-1}.

Electrochemical Tests: Electrochemical measurements were performed in a standard three-electrode glass cell on a 760 workstation (Pine Research Instruments, US) under ambient conditions. A Pt wire and an Ag/AgCl/KCl (3 M) were used as counter and reference electrodes, respectively. 1 mg of catalysts were ultrasonically dispersed in 970 µL of mixed solution of 2-proponal and Milli-Q water (1/3, v/v) with 30 µL of 0.1 % Nafion (15 wt% of Nafion in the catalyst), resulting in a catalyst concentration of 1 mg mL^{-1}. A portion of catalyst dispersion was then transferred onto the RDE via a controlled drop casting method, which yielded a loading of catalyst 0.1 mg cm^{-2}. The resulting electrode was dried under ambient conditions.

The overall electron transfer numbers per oxygen molecule involved in the typical ORR process were calculated from the slopes of the Koutecky-Levich plots using the following equations:[8,49]

$$\frac{1}{J} = \frac{1}{J_L} + \frac{1}{J_K} = \frac{1}{B\omega^{0.5}} + \frac{1}{J_K} \quad (1)$$

$$B = 0.62nFC_0(D_0)^{2/3}\nu^{-1/6} \quad (2)$$

$$J_K = nFkC_0 \quad (3)$$

in which J is the measured current density, J_K and J_L are the kinetic- and diffusion-limiting current densities, ω is the electrode rotating speed in rpm, and B is the reciprocal of the slope, n is the number of electrons transferred per oxygen molecule, F is the Faraday constant (F = 96 485 C mol^{-1}), C_0 is the concentration of O_2, D_0 is the diffusion coefficient of O_2, ν is the kinematic viscosity of the electrolyte, and k is the electron transfer rate constant. In this study, the electrolyte was O_2 saturated 0.1 M KOH, C_0, D_0 and ν were used as 1.2×10^{-3} M, 1.9×10^{-5} cm^2 s^{-1}, and 0.01 cm^2 s^{-1}, respectively. The constant 0.62 in Equation 2 was substituted by 0.2 when the rotating speed is expressed in rpm.

Supporting Information

Supporting Information is available from the Wiley Online Library or from the author.

Acknowledgements

This work was financially supported by the Australian Research Council (ARC) through the Discovery Project program (DP1095861, DP130104459).

Received: August 22, 2013
Revised: October 3, 2013
Published online: November 29, 2013

[1] Y. Li, Q. Liu, W. Shen, *Dalton Trans.* **2011**, *40*, 5811.
[2] K. Zhou, Y. Li, *Angew. Chem.* **2012**, *124*, 622; *Angew. Chem. Int. Ed.* **2012**, *51*, 602.
[3] M. K. Debe, *Nature* **2012**, *486*, 43.
[4] R. Cao, J. S. Lee, M. Liu, J. Cho, *Adv. Energy Mater.* **2012**, *2*, 816.
[5] S. H. Joo, S. J. Choi, I. Oh, J. Kwak, Z. Liu, O. Terasaki, R. Ryoo, *Nature* **2001**, *412*, 169.
[6] D. Wang, H. L. Xin, R. Hovden, H. Wang, Y. Yu, D. A. Muller, F. J. Disalvo, H. D. Abruña, *Nat. Mater.* **2013**, *12*, 81.
[7] R. Bashyam, P. Zelenay, *Nature* **2006**, *443*, 63.
[8] Y. Liang, Y. Li, H. Wang, J. Zhou, J. Wang, T. Regier, H. J. Dai, *Nat. Mater.* **2011**, *10*, 780.
[9] Z. S. Wu, S. Yang, Y. Sun, K. Parvez, X. L. Feng, K. Müllen, *J. Am. Chem. Soc.* **2012**, *134*, 9082.
[10] Y. F. Xu, M. R. Gao, Y. R. Zheng, J. Jiang, S. H. Yu, *Angew. Chem.* **2013**, *125*, 8708; *Angew. Chem. Int. Ed.* **2013**, *52*, 8546.
[11] M. R. Gao, Y. F. Xu, J. Jiang, Y. R. Zheng, S. H. Yu, *J. Am. Chem. Soc.* **2012**, *134*, 2930.
[12] Z. R. Tian, W. Tong, J. Y. Wang, N. G. Duan, V. V. Krishnan, S. L. Suib, *Science* **1997**, *276*, 926.
[13] M. K. Song, S. Cheng, H. Chen, W. Qin, K. W. Nam, S. Xu, X. Q. Yang, A. Bongiorno, J. Lee, J. Bai, T. A. Tyson, J. Cho, M. Liu, *Nano Lett.* **2012**, *12*, 3483.
[14] S. Guo, S. Zhang, L. Wu, S. Sun, *Angew. Chem.* **2012**, *124*, 11940; *Angew. Chem. Int. Ed.* **2012**, *51*, 11770.
[15] S. Yang, L. Zhi, K. Tang, X. L. Feng, J. Maier, K. Müllen, *Adv. Funct. Mater.* **2012**, *22*, 3634.
[16] D. Geng, Y. Chen, Y. Chen, Y. Li, R. Li, X. Sun, S. Ye, S. Knights, *Energy Environ. Sci.* **2011**, *4*, 760.
[17] J. Duan, Y. Zheng, S. Chen, Y. Tang, M. Jaroniec, S. Z. Qiao, *Chem. Commun.* **2013**, *49*, 7705.
[18] X. Xie, Y. Li, Z. Q. Liu, M. Haruta, W. Shen, *Nature* **2009**, *458*, 746.
[19] J. Wu, L. Qi, H. You, A. Gross, J. Li, H. Yang, *J. Am. Chem. Soc.* **2012**, *134*, 11880.
[20] V. R. Stamenkovic, B. Fowler, B. S. Mun, G. Wang, P. N. Ross, C. A. Lucas, N. M. Markovic, *Science* **2007**, *315*, 493.
[21] J. Xiao, Q. Kuang, S. Yang, F. Xiao, S. Wang, L. Guo, *Sci. Rep.* **2013**, *3*, 2300.
[22] Y. Liang, Y. Li, H. Wang, H. J. Dai, *J. Am. Chem. Soc.* **2013**, *135*, 2013.
[23] D. Deng, X. Pan, L. Yu, Y. Cui, Y. Jiang, J. Qi, W.-X. Li, Q. Fu, X. Ma, Q. Xue, G. Sun, X. H. Bao, *Chem. Mater.* **2011**, *23*, 1188.
[24] Z. Chen, Z. Jiao, D. Pan, Z. Li, M. Wu, C. H. Shek, C. M. Wu, J. K. Lai, *Chem. Rev.* **2012**, *112*, 3833.
[25] M. Liu, H. C. Zeng, *Cryst. Growth Des.* **2012**, *12*, 5561.
[26] T. Yu, J. Moon, J. Park, Y. I. Park, H. Bin Na, B. H. Kim, I. C. Song, W. K. Moon, T. Hyeon, *Chem. Mater.* **2009**, *21*, 2272.
[27] Y. A. Kim, K. Fujisawa, H. Muramatsu, T. Hayashi, M. Endo, T. Fujimori, K. Kaneko, M. Terrones, J. Behrends, A. Eckmann, C. Casiraghi, K. S. Novoselov, R. Saito, M. S. Dresselhaus, *ACS Nano* **2012**, *6*, 6293.
[28] J. Qu, F. Gao, Q. Zhou, Z. Wang, H. Hu, B. Li, W. Wan, X. Wang, J. Qiu, *Nanoscale* **2013**, *5*, 2999.
[29] J. Liang, Y. Jiao, M. Jaroniec, S. Z. Qiao, *Angew. Chem.* **2012**, *124*, 11664; *Angew. Chem. Int. Ed.* **2012**, *51*, 11496.
[30] D. Long, W. Li, L. Ling, J. Miyawaki, I. Mochida, S. H. Yoon, *Langmuir* **2010**, *26*, 16096.
[31] Y. Gorlin, T. F. Jaramillo, *J. Am. Chem. Soc.* **2010**, *132*, 13612.
[32] Z. Lin, M. K. Song, Y. Ding, Y. Liu, M. Liu, C. P. Wong, *Phys. Chem. Chem. Phys.* **2012**, *14*, 3381.
[33] P. Wu, Y. D. Qian, P. Du, H. Zhang, C. X. Cai, *J. Mater. Chem.* **2012**, *22*, 6402.
[34] J. Wang, J. Zhou, Y. Hu, T. Regier, *Energy Environ. Sci.* **2013**, *6*, 926.
[35] P. Li, C. Nan, Z. Wei, J. Lu, Q. Peng, Y. Li, *Chem. Mater.* **2010**, *22*, 4232.
[36] N. Wang, L. Guo, L. He, X. Cao, C. Chen, R. Wang, S. Yang, *Small* **2007**, *3*, 606.
[37] W. Z. Wang, C. K. Xu, G. H. Wang, Y. K. Liu, C. L. Zheng, *Adv. Mater.* **2002**, *14*, 837.
[38] H. P. Cong, S. H. Yu, *Cryst. Growth Des.* **2009**, *9*, 210.
[39] V. Bayer, R. Podloucky, C. Franchini, F. Allegretti, B. Xu, G. Parteder, M. Ramsey, S. Surnev, F. Netzer, *Phys. Rev. B* **2007**, *76*.
[40] Y. Tan, C. Xu, G. Chen, X. Fang, N. Zheng, Q. Xie, *Adv. Funct. Mater.* **2012**, *22*, 4584.
[41] L. Q. Mao, D. Zhang, T. Sotomura, K. Nakatsu, N. Koshiba, T. Ohsaka, *Electrochim. Acta* **2003**, *48*, 1015.
[42] J. Wu, D. Zhang, Y. Wang, Y. Wan, B. Hou, *J. Power Sources* **2012**, *198*, 122.
[43] Y. Liang, H. Wang, P. Diao, W. Chang, G. Hong, Y. Li, M. Gong, L. Xie, J. Zhou, J. Wang, T. Z. Regier, F. Wei, H. J. Dai, *J. Am. Chem. Soc.* **2012**, *134*, 15849.
[44] Y. Zheng, Y. Jiao, J. Chen, J. Liu, J. Liang, A. Du, W. Zhang, Z. Zhu, S. C. Smith, M. Jaroniec, G. Q. Lu, S. Z. Qiao, *J. Am. Chem. Soc.* **2011**, *133*, 20116.
[45] J. Liang, Y. Zheng, J. Chen, J. Liu, D. Hulicova-Jurcakova, M. Jaroniec, S. Z. Qiao, *Angew. Chem.* **2012**, *124*, 3958; *Angew. Chem. Int. Ed.* **2012**, *51*, 3892.
[46] M. Biswal, V. V. Dhas, V. R. Mate, A. Banerjee, P. Pachfule, K. L. Agrawal, S. B. Ogale, C. V. Rode, *J. Phys. Chem. C* **2011**, *115*, 15440.
[47] H. Huang, Q. Yu, X. Peng, Z. Ye, *Chem. Commun.* **2011**, *47*, 12831.
[48] W. S. Hummers, R. E. Offeman, *J. Am. Chem. Soc.* **1958**, *80*, 1339.
[49] U. A. Paulus, T. J. Schmidt, H. A. Gasteiger, R. J. Behm, *J. Electroanal. Chem.* **2001**, *495*, 134.